

A Joint *Chandra* and *XMM-Newton* View of Abell 3158: Massive Off-Centre Cool Gas Clump As A Robust Diagnostic of Merger Stage

Yu Wang¹, Haiguang Xu¹, Liyi Gu¹, Junhua Gu¹, Zhenzhen Qin¹,
Jingying Wang¹, Zhongli Zhang² and Xiang-Ping Wu³

¹Department of Physics, Shanghai Jiao Tong University, 800 Dongchuan Road, Shanghai 200240, PRC. E-mail: wenyu_wang@sjtu.edu.cn; hgxu@sjtu.edu.cn

²Max-Planck-Institute of Astrophysics, Karl-Schwarzschild-Str. 1, Postfach 1317 D-85741, Garching, Germany

³National Astronomical Observatories, Chinese Academy of Sciences, 20A Datun Road, Beijing 100012, PRC

Received October 22 / Accepted 30 December 2009

ABSTRACT

By analysing the *Chandra* and *XMM-Newton* archived data of the nearby galaxy cluster Abell 3158, which was reported to possess a relatively regular, relaxed morphology in the X-ray band in previous works, we identify a bow edge-shaped discontinuity in the X-ray surface brightness distribution at about $120h_{71}^{-1}$ kpc west of the X-ray peak. This feature is found to be associated with a massive, off-centre cool gas clump, and actually forms the west boundary of the cool clump. By calculating the thermal gas pressures in the cool clump and in the free-stream region, we determine that the cool gas clump is moving at a subsonic velocity of 700_{-340}^{+140} km s⁻¹ ($\mathcal{M} = 0.6_{-0.3}^{+0.1}$) toward west on the sky plane. We exclude the possibility that this cool clump was formed by local inhomogeneous radiative cooling in the intra-cluster medium, due to the effectiveness of the thermal conduction on the time-scale of ~ 0.3 Gyr. Since no evidence for central AGN activity has been found in Abell 3158, and this cool clump bears many similarities to the off-centre cool gas clumps detected in other merging clusters in terms of their mass, size, location, and thermal properties (e.g. lower temperature and higher abundance as compared with the environment), we speculate that the cool clump in Abell 3158 was caused by a merger event, and is the remnant of the original central cool-core of the main cluster or the infalling sub-cluster. This idea is supported not only by the study of line-of-sight velocity distribution of the cluster member galaxies, but also by the study of gas entropy-temperature correlation. This example shows that the appearance of such massive, off-centre cool gas clumps can be used to diagnose the dynamical state of a cluster, especially when prominent shocks and cold fronts are absent.

Key words: galaxies: clusters: individual (Abell 3158) – X-rays: galaxies: clusters – intergalactic medium – kinematics and dynamics

1 INTRODUCTION

In the frame of hierarchical clustering scenario, galaxy clusters grow in size by merging with subunits, with each major merger event lasting for 2 – 5 Gyr (e.g. Roettiger, Loken & Burns 1997; Ascasibar & Markevitch 2006; Poole et al. 2006). In such major mergers both ram pressure stripping and slingshot can generate remarkable X-ray substructures in gas density and temperature distributions, which are often accompanied by shocks and/or cold fronts that exhibit arc-shaped or edge-like morphologies (e.g. Markevitch & Vikhlinin 2007 and references therein). These substructures are expected to contain valuable information not only on merger dynamics itself, but also on thermal and chemical evolutions of the

hot intra-cluster medium (ICM), which helps understand the nature of dark matter (Markevitch et al. 2004; Randall et al. 2008).

Theoretical studies and numerical N-body simulations (e.g. Roettiger et al. 1997; Ricker 1998; Poole et al. 2006) showed that in a typical major merger event temperature substructures may survive for a relatively long time of $t_{\text{thermal}} \simeq n_{\text{gas}} kT / n_{\text{gas}}^2 \Lambda$, where n_{gas} , T , and Λ are gas density, temperature, and cooling function, respectively. The derived t_{thermal} (up to about 4 Gyr in some cases) is much longer than the lifetimes of shocks and cold fronts, since shocks and cold fronts are usually smeared out quickly on dynamic time-scales characterized by the sound crossing time. Actually, high-quality *Chandra* and *XMM-Newton* observations have shown that in merging clusters there is a prevailing existence of

massive, off-centre cool gas clumps, which are about 50 – 300 kpc in size, reside within the central ($\lesssim 600$ kpc) region of the cluster, and possess an average temperature 1 – 4 keV lower than the ambient gas.

In 1E 0657 – 56 (the Bullet cluster; Markevitch et al. 2002), Abell 520 (Govoni et al. 2004), Abell 2256 (Sun et al. 2002), and Abell 3667 (Vikhlinin, Markevitch & Murray 2001), the off-centre cool gas clump is found to be moving adiabatically behind a bow shock and/or a cold front, and thus can be directly identified as the remnant of the original central cool-core of the infalling sub-cluster. On the other hand, in clusters such as Abell 754 (Markevitch et al. 2003), Abell 2065 (Chatzikos, Sarazin & Kempner 2006), and Abell 2255 (Sakelliou & Ponman 2006), the off-centre cool gas clump is not escorted by either a shock or a cold front. However, unambiguous evidence obtained in radio, optical, and X-ray bands still indicates that the cool gas clump was driven out of the core region of either the main cluster (Abell 754; Markevitch et al. 2003; Henry, Finoguenov & Briel 2004) or the infalling sub-cluster by the merger.

In fact, the off-centre cool gas clumps in above two types of clusters share many similarities in terms of their sizes, locations, and gas masses ($\sim 10^{11} M_{\odot}$). Therefore, an interesting question arises: can the appearance of such massive, off-centre cool gas clumps be safely used to diagnose the dynamical state of a cluster, even when there is a lack of violent merger signatures, such as prominent shocks, cold fronts, and other associated radio/optical substructures? Clearly, in order to address this issue, we need to examine gas temperature distribution in more galaxy clusters that show only weak merger signatures and have evolved into late merger stages (usually mean post core passages).

In this work we present a detailed joint *Chandra* and *XMM-Newton* study of the nearby rich galaxy cluster Abell 3158 (richness class 2, Quintana & Halven 1979; $z = 0.0597$, Struble & Rood 1999), which contains 105 member galaxies within the central $2.4h_{71}^{-1}$ Mpc (Biviano et al. 2002). In literature (e.g. Irwin, Bregman & Evrard 1999; Lokas et al. 2006; Chen et al. 2007), this cluster is usually referred as a relaxed, non-cool-core system, because neither significant X-ray substructures nor diffuse radio emission has been reported in the previous works (Ku et al. 1983; Mohr, Mathiesen & Evrard 1999; Schuecker et al. 2001; Mauch et al. 2003). In the optical band, however, the cluster shows some unusual properties that can be possibly related to a recent merger event, as are summarized as follows. First, the cluster hosts three luminous elliptical galaxies that are brighter than $9 \times 10^{10} L_{B,\odot}$ (Paturel et al. 2003), all classified as a cD galaxy by Sérsic (1974). Two of them, the brightest member PGC 13641 (E0, $L_B = 1.45 \times 10^{11} L_{B,\odot}$) and the S0 galaxy PGC 13652 ($L_B = 9.39 \times 10^{10} L_{B,\odot}$), constitute a closely aligned central galaxy pair, whose projected separation is $81.3h_{71}^{-1}$ kpc, and jointly dominate the cluster (Quintana & Havlen 1979). The second luminous member PGC 13679 (S0, $L_B = 9.48 \times 10^{10} L_{B,\odot}$) is located at about $417.8h_{71}^{-1}$ kpc southeast of the central galaxy pair, and dominates a local sub-cluster whose recessional velocity is about 1 300 km s $^{-1}$ larger than the mean recessional velocity of the main cluster (17 500 km s $^{-1}$; Lucey et al. 1983; Kolokotronis et al. 2001). Second, as shown in figure 7 of Smith et al. (2004), the line-of-sight velocity distribution of the cluster’s member galaxies exhibits a plateau at the high-velocity end, which is often seen in merging systems. Third, Kolokotronis et al. (2001) reported that in this cluster there is an offset of about $200h_{71}^{-1}$ kpc between the optical flux-weighted centroid and the optical density peak. Based on these we speculate that

Abell 3158 is evolving at a late merger stage and is thus an ideal target for our investigation.

Throughout the paper, we adopt the cosmological parameters $H_0 = 71$ km s $^{-1}$ Mpc $^{-1}$, $\Omega_M = 0.27$, and $\Omega_{\Lambda} = 0.73$, so that 1'' corresponds to about $1.14h_{71}^{-1}$ kpc at the redshift of the cluster. We utilize the solar abundance standards given by Grevesse and Sauval (1998), where the iron abundance relative to hydrogen is 3.16×10^{-5} in number. Unless stated otherwise, the quoted errors are the 90% confidence limits.

2 OBSERVATIONS AND DATA REDUCTIONS

2.1 *Chandra*

Except for an extremely short exposure on 2007 September 16 (5.1 ks, ObsID 7688), which is not used in this work, Abell 3158 has also been observed with *Chandra* on 2002 June 19 (31.4 ks, ObsID 3712) and June 21 (25.1 ks, ObsID 3201), respectively, with chips 0, 1, 2, 3, and 6 of the Advanced CCD Imaging Spectrometer (ACIS) operating in VFAINT mode. We used the *Chandra* data analysis package CIAO version 4.1 and CALDB version 4.1.2 to process the archived data in the standard way, by starting with the level-1 event files. Corrections for the charge transfer inefficiency and time dependent gain have been applied. We kept events with ASCA grades 0, 2, 3, 4, and 6, and removed all the bad pixels, bad columns, and columns adjacent to bad columns and node boundaries. We examined the 0.3 – 10.0 keV lightcurves extracted from the background regions defined on ACIS chips 0 and 1, and found that there are no strong flares that increase the background count rate to $> 120\%$ of the mean quiescent value. The obtained net exposures are 30.9 ks and 24.8 ks for the two observations, respectively. In the spectral analysis, we extracted the *Chandra* spectra in 0.7 – 8.0 keV from the two observations separately, and fitted them simultaneously with the same model, except that their normalizations were left free. Background spectra were extracted from the *Chandra* blank-sky fields; a crosscheck based on the use of local background yielded essentially the same results.

2.2 *XMM-Newton*

Abell 3158 was observed with *XMM-Newton* on 2005 November 22 (22.4 ks, ObsID 0300210201) and 2006 January 18 (9.4 ks, ObsID 0300211301), respectively, with the European Photon Imaging Camera (EPIC) operating in PrimeFullWindow (MOS1 and MOS2) and PrimeFullWindowExtended (pn) modes. Although during the second observation the Reflection Grating Spectrometer (RGS) was also turned on, in this work we limited our analysis to the first observation only by using the latest version of SAS (version 8.0.1) and its standard filterings. We kept the events with FLAG=0 and PATTERNS 0 – 12 for MOS1 and MOS2, and the events with FLAG=0 and PATTERNS 0 – 4 for pn. We removed all the time intervals contaminated by soft proton flares, during which the 10 – 12 keV count rate exceeds the 2σ limit of the mean quiescent value (see, e.g. Katayama et al. 2004). The cleaned MOS1, MOS2, and pn datasets have effective exposure times of 20.9 ks, 20.6 ks, and 12.2 ks, respectively. In the spectral analysis, we removed all the bright X-ray point sources and adopted conservative energy cuts at 0.5 keV and 8.0 keV. The obtained MOS1, MOS2, and pn spectra were fitted simultaneously using the same model, except that their normalizations were left free. Backgrounds spectra were generated from the blank-sky event lists, which were filtered in advance using the same

selection criteria (PATTERN, FLAG, etc.) as used for the source spectra.

3 X-RAY ANALYSIS AND RESULTS

3.1 X-ray surface brightness discontinuity

In Fig. 1a and 1b, we show the *Chandra* ACIS and combined *XMM-Newton* EPIC images of the central $1.5h_{71}^{-1} \text{ Mpc} \times 1.5h_{71}^{-1} \text{ Mpc}$ ($21'.9 \times 21'.9$) region of Abell 3158 in 0.3 – 2.0 keV, respectively, which have been adaptively smoothed and corrected for both exposure and vignetting. The *XMM-Newton* image was generated by combining the MOS1, MOS2, and PN events together using the SAS ‘image’ script. The X-ray peak of the cluster (R.A.=03h42m52.7s Dec=−53d37m37.2s J2000) is found at about $17.8h_{71}^{-1} \text{ kpc}$ ($0'.26$) northwest of the optical centroid of PGC 13641 (R.A.= 03h42m52.9s Dec=−53d37m52.2s; Katgert et al. 1998), the brighter member of the central galaxy pair. The corresponding optical Digital Sky Survey (DSS) image is shown in Fig. 1c, on which the *Chandra* intensity contours obtained from Fig. 1a are overlaid.

On both *Chandra* and *XMM-Newton* images it can be clearly seen that the X-ray isophotes are elongated in nearly the east-west direction with an ellipticity of $\simeq 0.3$. And on the *Chandra* image a bow edge can be identified at about $120h_{71}^{-1} \text{ kpc}$ ($1'.88$) west of the X-ray peak. According to its shape and location on the detector, the possibility of the feature being associated with the artifacts caused by CCD gaps or bad columns can be excluded.

In order to examine the significance of the bow edge in a quantitative way, we define two sets of partial elliptical annuli, which are confined in the east and west sector regions shown in Fig. 2a, and extract the exposure-corrected X-ray surface brightness profiles (SBPs) with both *Chandra* ACIS and *XMM-Newton* EPIC (Fig. 2b). Because the gas temperature of Abell 3158 is sufficiently high (5.8 keV; Reiprich & Böhringer 2002), by following, e.g. Markevitch et al. (2000), we restricted the SBP extractions in 0.3 – 2.0 keV to minimize the dependence of X-ray emissivity on possible temperature fluctuations (see §3.2). We attempt to apply the standard β model to describe the extracted SBPs, which is expressed as

$$S(r) = S_0[1 + (r/r_c)^2]^{0.5-3\beta} + S_{\text{bkg}} \quad (1)$$

(Jones & Forman 1984), where r_c is the core radius, β is the slope, S_{bkg} is the background, and S_0 is the normalization. We find that in the east sector the SBPs can be fitted very well with the β model (Table 1), whereas in the west sector the SBPs show a significant central excess beyond the best-fit β model for the outer ($> 120h_{71}^{-1} \text{ kpc}$) regions. Within about $90h_{71}^{-1} - 115h_{71}^{-1} \text{ kpc}$ ($1'.32 - 1'.68$), where the bow edge is identified visually, there exists a sudden discontinuity, across which the *Chandra* and *XMM-Newton* surface brightness increases inwards by a factor of $\simeq 1.6$ and $\simeq 1.3$, respectively; this difference may be caused by the different distributions of the point spread function (PSF) of *Chandra* ACIS and *XMM-Newton* EPIC. These results confirm the existence of the bow edge shown in Fig. 1a, and indicate that it is not related to the central surface brightness excess usually seen in the cD galaxies (Makishima et al. 2001), which are not associated with a surface brightness discontinuity. Also, we note that the X-ray surface brightness discontinuity in Abell 3158 is similar to, although not as sharp as, those found in 1E 0657 – 56 and Abell 3667, in which the jumps of the surface brightness at the edges are 2 – 3 within $\simeq 10h_{71}^{-1}$

kpc and thus the edges have been confirmed as cold fronts caused by mergers (Markevitch et al. 2002; Vikhlinin et al. 2001).

3.2 An unusual off-centre cool gas clump

In order to investigate the thermal properties of the bow edge, we calculate the two dimensional gas temperature distribution in the central $0.6h_{71}^{-1} \text{ Mpc} \times 0.6h_{71}^{-1} \text{ Mpc}$ ($8'.77 \times 8'.77$) region of Abell 3158, by following the approach of, e.g. O’Sullivan et al. (2005) and Gu et al. (2009). In the calculation only the *XMM-Newton* EPIC datasets are used, because the data statistics of the *Chandra* ACIS datasets is not good enough for us to map the temperature distribution. To be specific, we first define about 4000 cells in the $0.6h_{71}^{-1} \text{ Mpc} \times 0.6h_{71}^{-1} \text{ Mpc}$ region, whose centres (\mathbf{r}_i , $i = 1, 2, 3, \dots$) are randomly distributed with a separation of $< 10''$ between the centres of any two adjacent cells. Each cell is apportioned with an adaptive radius of $0'.3 - 0'.8$, so that it encloses > 3000 photons in 0.5 – 8.0 keV after the point sources are excluded. Then we extract the MOS1, MOS2, and pn spectra from each cell and fit them simultaneously with an absorbed APEC model coded in XSPEC v12.4.0. The redshift and absorption are fixed to $z = 0.0597$ and the Galactic value $N_{\text{H}} = 1.62 \times 10^{20} \text{ cm}^{-2}$ (Dickey & Lockman 1990), respectively. After the obtained best-fit gas temperature is assigned to the corresponding cell ($T_c(\mathbf{r}_i)$), and this process is repeated for all cells, we calculate the projected temperature at any position \mathbf{r} as

$$T(\mathbf{r}) = \sum_{\mathbf{r}_i} [G_{\mathbf{r}_i}(R_{\mathbf{r},\mathbf{r}_i})T_c(\mathbf{r}_i)] / \sum_{\mathbf{r}_i} G_{\mathbf{r}_i}(R_{\mathbf{r},\mathbf{r}_i}), \quad R_{\mathbf{r},\mathbf{r}_i} < s(\mathbf{r}_i) \quad (2)$$

(Gu et al. 2009), where $R_{\mathbf{r},\mathbf{r}_i}$ is the distance between \mathbf{r} and the centre of the cell i , $s(\mathbf{r}_i)$ is defined as the radius of cell i , and $G_{\mathbf{r}_i}$ is the Gaussian kernel with a scale parameter $\sigma = s(\mathbf{r}_i)$. The obtained temperature map, along with the 1σ error map that is calculated in nearly the same way as the temperature map, are shown in Fig. 3a and 3b, respectively.

We find that, despite the relatively regular appearance of the X-ray images (Fig. 1), the spectral distribution of the projected gas temperature is highly asymmetric, inferring that the cluster has not recovered from a violent event on cluster scales. In particular, we find that there exists a cool gas clump at about $84h_{71}^{-1} \text{ kpc}$ ($1'.23$) west of the X-ray peak, whose linear scale is about $80h_{71}^{-1} \text{ kpc}$ ($1'.17$). The projected gas temperature within this cool clump ranges from about 4.4 keV to 5.0 keV, which is apparently lower than that of the ambient gas (5.2 – 6.0 keV). Most interestingly, the west boundary of the cool gas clump coincides with the bow edge perfectly, indicating that they are likely to have the same origin.

To clarify the significance of the existence of the cool gas clump, we define four sector regions in Fig. 3a, two of which have the same angles as those defined earlier in Fig. 2a, and divide each of these sector regions into a series of wider partial elliptical annuli. We extract both the *Chandra* ACIS and *XMM-Newton* MOS1, MOS2, and pn spectra from these annuli, and fit them with an absorbed APEC model when the redshift and absorption are fixed again as above; allowing the absorption to vary does not improve the fits. In the fittings, the *Chandra* ACIS spectra extracted from the two observations are treated as group one, and the *XMM-Newton* MOS1, MOS2 and pn spectra are treated as group two. Each group of spectra are fitted simultaneously with the same model parameters, except for that the normalizations are left free. The derived projected temperature profiles in the four sectors are plotted in Fig. 4a – 4d. It can be clearly seen that the *Chandra* and *XMM-Newton*

temperatures are consistent with each other (68% confidence level), and in the west sector the temperature in $45.4 - 95.3h_{71}^{-1}$ kpc (4.85 ± 0.17 keV), where the cool gas clump is located, is lower than those of the adjacent regions at 68% confidence level (see also Table 2); no such temperature drop is found in other three directions. This is further confirmed by the results of the deprojected analysis of the *XMM-Newton* spectra for the west sector (Table 2 and Fig. 4e – 4f), which shows that the gas temperature of the cool gas clump ($3.98_{-0.41}^{+0.43}$ keV for W2 region) is actually lower than those of the innermost region ($5.71_{-0.71}^{+1.04}$ keV for W1 region) and the next outer region ($5.38_{-0.51}^{+0.74}$ keV for W3 region) at the 90% confidence level, and cannot be ascribed to the uncertainties in determining the metal abundance.

3.3 Faint Cold front associated with the cool gas clump

To study the nature of the cool gas clump, we carry out a simple hydrodynamic study to determine the velocity of the edge in the environment. By applying the best-fit deprojected spectral parameters (Table 2), here we revisit the X-ray surface brightness profiles of the west sector (Fig. 2b) and fit it again with two models. In the first model (model A), the spatial distribution of gas density is described with two β components as

$$n_{\text{gas}}(R) = \{n_{g,1}^2[1+(R/R_{c1})^2]^{-3\beta_1} + n_{g,2}^2[1+(R/R_{c2})^2]^{-3\beta_2}\}^{1/2}, \quad (3)$$

where R is the 3-dimensional radius, R_c is the core radius, and β is the slope. In the second model (model B), the gas density distribution is broken at the truncation radius R_{cut} , described with one truncated power-law component and one truncated β component as

$$n_{\text{gas}}(R) = \begin{cases} n_{g,1}(R/R_{\text{cut}})^{-\alpha} & R < R_{\text{cut}} \\ n_{g,2}[1+(R/R_c)^2]^{-3\beta/2} & R \geq R_{\text{cut}} \end{cases}. \quad (4)$$

Acceptable fits to both the *Chandra* and *XMM-Newton* SBPs can be obtained with model B only (Table 1). The *Chandra* best-fit suggests a density jump by a factor of $f_{\text{jump}} = 1.7 \pm 0.1$ at $R_{\text{cut}} = 111.0 \pm 4.4h_{71}^{-1}$ kpc (roughly the position of the edge), and the *XMM-Newton* best-fit gives consistent values of $f_{\text{jump}} = 1.5 \pm 0.1$ and $R_{\text{cut}} = 104.9 \pm 2.2h_{71}^{-1}$ kpc.

Following Vikhlinin et al. (2001), we use the best-fit gas densities across the edge (Eq.(4)) and gas temperatures for W2 and W3 regions (§3.2 and Fig. 4e) to calculate the thermal gas pressures in the cool gas clump (P_0) and in the free-stream region (P_1), respectively. The former pressure is assumed to be in pressure equilibrium with the gas pressure at the stagnation point (denoted as the place where the relative gas velocity vanishes). The pressure ratio is estimated to be $P_0/P_1 = 1.3 \pm 0.2$ (68% confidence level). This allows us to determine the Mach number (\mathcal{M}) of the cool clump to be $0.6_{-0.3}^{+0.1}$, which corresponds to a velocity of 700_{-340}^{+140} km s⁻¹. This subsonic velocity of the clump, along with the results obtained in §3.1 (i.e., surface brightness discontinuity) and §3.2 (i.e., gas temperature and density discontinuities), allow us to conclude that there exists a faint cold front at the west boundary of the cool gas clump.

4 VELOCITY PLATEAU

In early works of Biviano et al. (1997 and 2002), Girardi et al. (1996), and Kolokotronis et al. (2001), both the two dimensional spatial distribution and the line-of-sight velocity distribution of the member galaxies in Abell 3158 were studied, and no significant

substructure was reported. However, after tighter and more reliable selection criterion for member galaxies, which was based on the galaxy colour-magnitude relation (e.g. Colless & Dunn 1996; Ferrari et al. 2003; Maurogordato et al. 2008), was applied, Smith et al. (2004) re-constructed the line-of-sight velocity distribution with higher fidelity and found that there exists a visible plateau beyond the Gaussian distribution at the high-velocity side. Since Smith et al. (2004) did not use a quantitative approach to assess the significance of the high-velocity plateau, in which the merger information might be contained, here we draw the velocity data of the member galaxies in Abell 3158 from Smith et al. (2004), and re-analyse the line-of-sight velocity distribution profile. After the model fitting of this distribution is finished, we also attempt to investigate the 2-dimensional spatial distribution of the galaxies in the high-velocity plateau.

First, we plot the line-of-sight velocity distribution of the 68 member galaxies identified by Smith et al. (2004) in Fig. 5a, which shows that the high-velocity plateau is located at about 19 000 km s⁻¹. We fit the observed distribution with a single Gaussian profile, and calculate the Kolmogorov–Smirnov statistic for the observed distribution against the best-fit Gaussian model ($\chi^2/dof = 31.6/9$). We find that the observed distribution has a probability of < 10% of being Gaussian. We then attempt to fit the observed distribution with a two-Gaussian model. The best-fit ($\chi^2/dof = 9.8/6$) gives an average velocity of $\langle v_1 \rangle = 17\,380 \pm 50$ km s⁻¹ and a corresponding variance of $\sigma_{v,1} = 520 \pm 50$ km s⁻¹ for the main Gaussian component, and $\langle v_2 \rangle = 19\,120 \pm 130$ km s⁻¹ and $\sigma_{v,2} = 510 \pm 100$ km s⁻¹ for the high-velocity plateau. By applying the F-test and the Kaye’s Mixture Model (KMM; McLachlan & Basford 1988; Ashman, Bird & Zepf 1994) test, the latter of which is based on a maximum likelihood algorithm, we find that the second Gaussian component is required at 94.3% confidence level and preferred at a significant probability of 90%, respectively.

To investigate if the galaxies in the high-velocity plateau form a real substructure in the cluster, we divide the member galaxies into two subgroups: one low-velocity (15 300 – 18 500 km s⁻¹) subgroup and one high-velocity (18 500 – 20 000 km s⁻¹) subgroup, which consist of 51 and 17 galaxies, respectively. According to the best-fit two-Gaussian model, these two subgroups roughly corresponds to the two Gaussian components, respectively, with up to about two of the galaxies in the high-velocity subgroup coming from the main Gaussian component. We find that the galaxies belonging to the high-velocity subgroup are distributed mostly in the central $500h_{71}^{-1}$ kpc (7'.3), as well as the west part of the cluster, with a geometric centroid of the high-velocity galaxies is located at about $355h_{71}^{-1}$ kpc (5'.2) northwest of the X-ray peak, which is not coincident with any X-ray substructures or luminous member galaxies. The high-velocity subgroup roughly includes the member galaxies of the PGC 13679 sub-cluster, since the member galaxies and the boundary of the latter are difficult to be determined by 2-dimensional spatial distribution alone (e.g. Colless & Dunn 1996; Boschin et al. 2006). The galaxies in the low-velocity subgroup that is dominated by the central PGC 13641-PGC 13652 galaxy pair, on the other hand, are scattered symmetrically in the field. These results suggest that the galaxy velocity separation (Fig. 5a; see also Smith et al. 2004) has a dynamical nature, which is most likely to be a major merger, with a merger mass ratio of about 1 : 1 – 3, as estimated from the velocity variance ratio ($\sigma_{v,2}/\sigma_{v,1} \simeq 1 : 1$) and the galaxy number ratio ($\simeq 17/51 = 1 : 3$) of the two subgroups.

In literature Abell 3158 was classified as a ‘single-component’ and ‘relaxed’ system (Kolokotronis et al. 2001; Lokas et al. 2006), which possesses a relatively regular morphology in the X-ray band

(Ku et al. 1983; Mohr et al. 1999; Schuecker et al. 2001). However, considering none of violent merger signatures is detected in the cluster, the existence of the high-velocity subgroup indicates that the cluster is evolving into the late stage of a major merger event. This may explain the origin of the off-centre cool gas clump detected in the west sector region, which is moving at a subsonic velocity (§3.2–§3.3; see also §5.1).

5 DISCUSSION

5.1 Merging origin of the massive, off-centre cool gas clump

The most prominent X-ray feature detected in Abell 3158 is the massive, off-centre cool gas clump, which is moving behind a **faint** cold front. It does not resemble the cool substructures caused by AGN activity (e.g. Forman et al. 2005; Nulsen et al. 2002), which are usually tightly associated with the low-density regions such as the AGN-induced radio lobes and X-ray cavities, since no evidence for AGN activity and its remnants has been reported in Abell 3158 according to the existing multi-band observations. In such a sense, we speculate that the cool clump was formed either by the inhomogeneous radiative cooling in the ICM, or by the ram pressure stripping or slingshot during a merger event. The first possibility can be ruled out immediately, because given the best-fit spectral parameters for the cool clump, the radiative cooling time of the gas in the clump (cf. Sarazin 1986) is

$$t_{\text{cool}} = 3.5 \times 10^{10} \text{ yr} \times \left(\frac{n_{\text{gas}}}{2 \times 10^{-3} \text{ cm}^{-3}} \right)^{-1} \times \left(\frac{kT}{10 \text{ keV}} \right)^{1/2} \simeq 9.8 \text{ Gyr}, \quad (5)$$

where continuum and line emissions are both included. This is close to the Hubble time ($\simeq 12.9$ Gyr) of the cluster, and is significantly longer than the Coulomb conduction time

$$t_{\text{cond}} \sim 9.2 \times 10^6 \text{ yr} \times \left(\frac{n_{\text{gas}}}{2 \times 10^{-3} \text{ cm}^{-3}} \right) \times \left(\frac{l}{100 \text{ kpc}} \right)^2 \left(\frac{kT_{\text{centre}}}{10 \text{ keV}} \right)^{-5/2} \simeq 0.06 \text{ Gyr} \quad (6)$$

(Markevitch et al. 2003), where $l = 80h_{71}^{-1}$ kpc is the linear scale of the cool clump, $kT_{\text{centre}} = 5.5 \pm 0.1$ keV is the average gas temperature for the cluster's central $200h_{71}^{-1}$ kpc ($2'.92$) region. If the conduction is suppressed by a factor of 5 due to the tangled magnetic field in the ICM (e.g. Narayan & Medvedev 2001; Zakamska & Narayan 2003; Chandran & Maron 2004), the effective conduction time increases to 0.3 Gyr. Consequently, even if the cool gas clump was formed through radiative cooling, it would have been destroyed very quickly by conduction, which indicates that the cool gas clump is most likely caused by merger. The same conclusions also hold for off-centre cool gas clumps found in other merging clusters (Table 3).

Assuming that the cool gas clump in Abell 3158 has a spherical geometry with a diameter of $80 - 110h_{71}^{-1}$ kpc (Fig. 3a), and has a constant density, the gas mass is estimated to be about $3.0 - 7.7 \times 10^{10} M_{\odot}$. This value is comparable to masses of the off-centre cool clumps identified in other merging clusters, which range from about $2.0 \times 10^{10} M_{\odot}$ to $1.3 \times 10^{12} M_{\odot}$ (Table 3). It also falls into the gas mass range of the cool-core regions of poor clusters and massive groups (e.g. Mulchaey et al. 1996; Gastaldello et al. 2007; Baldi et al. 2009). In fact, as shown in Table 3, not only the

gas mass, but also the size, temperature gradient, and the relatively high metal abundance of the cool clump in Abell 3158 resemble those of other off-centre cool clumps detected in 1E 0657 – 56 (Markevitch et al. 2002), Abell 754 (Markevitch et al. 2003), Abell 2065 (Chatzikos et al. 2006), Abell 2255 (Sakellidou & Ponman 2006), Abell 2256 (Sun et al. 2002), and Abell 3667 (Vikhlinin et al. 2001). Note that most of the off-centre cool clumps in these merging systems are considered to be the remnant of the cool-core of either the main cluster or the infalling sub-cluster. Based on all these similarities, it is natural to speculate that the cool gas clump in Abell 3158 was formed by the ram pressure stripping or slingshot during a merger event.

The above speculation is enhanced by the study of the correlation between gas temperature and entropy, which is defined as $S = kT/n_{\text{gas}}^{2/3}$ in terms of gas temperature kT and density n_{gas} . By quoting the data of Zhang et al. (2007) and Sanderson, O'Sullivan & Ponman (2009), we re-calculate the redshift-corrected gas entropy at $0.1R_{500}$ (R_{500} is the radius at which the mean over-density is 500 with respect to the critical density of the universe) for a sample of 13 cool-core clusters and a sample of 19 non-cool-core clusters. We also calculate the gas entropy of the seven cool gas clumps listed in Table 3. The entropy-temperature distribution is plotted in Fig. 6, where the strong correlations for the cool-core and non-cool-core clusters are characterized by two power-law models, respectively (Sanderson et al. 2009). It can be clearly seen that cool gas clumps in Abell 3158 and most of other merging clusters follow the relation for cool-core clusters, which reveals their nature as cool-core remnants. Note that the gas entropy of the cool clump in 1E 0657-56 is significantly below the relation for cool-core clusters at least 1σ limit (Fig. 6), which is possibly due to that the cool clump is compressed extremely as it experiences the ram pressure stripping force and passes through the deep potential of the main cluster during this drastic high-velocity merger event (Markevitch et al. 2002).

Based on above data analysis, calculations, and discussions, we propose that the appearance of the massive off-centre cool gas clumps can be regarded as a robust diagnostic of merger state. Combining the study of cold fronts (e.g. Owers et al. 2009), which survive longer than the shocks, with the study of such cool gas clumps, we may be able to place tight constraints on the merger history.

5.2 Possible merging scenarios

In Abell 3158, the X-ray bow edge of the faint cold front is pointing towards west in projection (§3.1–§3.3), which indicates that the symmetrical axis of the merging process is reasonably close to the west-east direction, although the projected effect lowers the detectability of the edge. The direction is also roughly consistent with the extending direction of the three cD galaxies (Fig. 1a), as well as the galaxy distribution of the high-velocity subgroup (Fig. 5b). Straightforwardly, the high-velocity subgroup has already made its closest approach to the core of the main cluster roughly from east to west. In this scenario, the apparent discrepancy between the moving velocity of the cool gas clump (700_{-340}^{+140} km s⁻¹; §3.3) and the relative line-of-sight velocity of the high-velocity subgroup (1740 ± 180 km s⁻¹; §4) demonstrates the gas component of the high-velocity subgroup possibly has been significantly slowed by the ram pressure stripping force. Regarding the late stage of the major merger (§4), perhaps the high-velocity subgroup is in its second core passage. On the other hand, because the three cD galaxies all lie well behind the cold front (Fig. 1a), perhaps the cluster is

in another merging scenario, in which the cool gas clump has been slingshot out from the centre of the main cluster, as expected after core passage, although the optical centroid of the high-velocity subgroup is not behind the faint cold front edge.

6 SUMMARY

By analysing the *Chandra* and *XMM-Newton* data of the nearby galaxy cluster Abell 3158, we identify a massive, off-centre cool gas clump, which is moving at a velocity of $\mathcal{M} = 0.6_{-0.3}^{+0.1}$, toward west on the sky plane behind a faint cold front. The possibilities of this substructure being formed by inhomogeneous radiative cooling and by central AGN activity are excluded. Based on the results obtained in the X-ray and optical analysis, we speculate that the cool gas clump is the remnant of the original central cool-core of the main cluster or the infalling sub-cluster during a major merger event. This case shows that the appearance of such massive, off-centre cool gas clumps can be used to diagnose the dynamical state of a cluster, especially when violent merger signatures (e.g. prominent shocks and cold fronts) are absent.

ACKNOWLEDGMENTS

We thank the *Chandra* and *XMM-Newton* teams for making this research. This work was supported by the National Science Foundation of China (Grant No. 10673008, 10878001 and 10973010), the Ministry of Science and Technology of China (Grant No. 2009CB824900/2009CB24904), and the Ministry of Education of China (the NCET Program).

REFERENCES

- Ascasibar Y., Markevitch M., 2006, *ApJ*, 650, 102
 Ashman K. M., Bird C. M., Zepf S. E., 1994, *AJ*, 108, 2348
 Baldi A., Forman W., Jones C., Nulsen P., David L., Kraft R., Simionescu A., 2009, *ApJ*, 694, 479
 Biviano A., Katgert P., Mazure A., Moles M., den Hartog R., Perea J., Focardi P., 1997, *A&A*, 321, 84
 Biviano A., Katgert P., Thomas T., Adami C., 2002, *A&A*, 387, 8
 Boschin, W., Girardi, M., Spolaor, M., Barrena, R., 2006, *A&A*, 449, 461
 Chandran B. D. G., Maron J. L., 2004, *ApJ*, 603, 23
 Chatzikos M., Sarazin C. L., Kempner J. C., 2006, *ApJ*, 643, 751
 Chen Y., Reiprich T. H., Böhringer H., Ikebe Y., Zhang Y.-Y., 2007, *A&A*, 466, 805
 Colless M., Dunn A. M., 1996, *ApJ*, 458, 435
 Dickey J. M., Lockman F. J., 1990, *ARA&A*, 28, 215
 Ferrari C., Maurogordato S., Cappi A., Benoist C., 2003, *A&A*, 399, 813
 Forman W., Nulsen P., Heinz S., Owen F., Eilek J., Vikhlinin A., Markevitch M., Kraft R., Churazov E., Jones C., 2005, *ApJ*, 635, 894
 Gastaldello F., Buote D. A., Humphrey P. J., Zappacosta L., Bullock J. S., Brighenti F., Mathews W. G., 2007, *ApJ*, 669, 158
 Girardi M., Fadda D., Giuricin G., Mardirossian F., Mezzetti M., Biviano A., 1996, *ApJ*, 457, 61
 Govoni F., Markevitch M., Vikhlinin A., VanSpeybroeck L., Ferretti L., Giovannini G., 2004, *ApJ*, 605, 695
 Grevesse N., Sauval A.J., 1998, *SSRv*, 85, 161
 Gu L., Xu H., Gu J., Wang Y., Zhang Z., Wang J., Qin Z., Cui H., Wu X.-P., 2009, accepted by *ApJ*
 Henry J. P., Finoguenov A., Briel U. G., 2004, *ApJ*, 615, 181
 Irwin J. A., Bregman J. N., Evrard A. E., 1999, *ApJ*, 519, 518
 Jones C., Forman W., 1984, *ApJ*, 276, 38
 Katayama H., Takahashi I., Ikebe Y., Matsushita K., Freyberg M. J., 2004, *A&A*, 414., 767
 Katgert P., Mazure A., den Hartog R., Adami C., Biviano A., Perea J., 1998, *A&AS*, 129, 399
 Kolokotronis V., Basilakos S., Plionis M., Georgantopoulos I., 2001, *MNRAS*, 320, 49
 Ku W. H.-M., Abramopoulos F., Nulsen P. E. J., Fabian A. C., Stewart G. C., Chincarini G. L., Tarengi M., 1983, *MNRAS*, 203, 253
 Lokas E. L., Wojtak R., Gottlöber S., Mamon G. A., Prada F., 2006, *MNRAS*, 367, 1463
 Lucey J. R., Dickens R. J., Mitchell R. J., Dawe J. A., 1983, *MNRAS*, 203, 545
 Makishima K., Ezawa H., Fukuzawa Y., Honda H., Ikebe Y., Kamae T., Kikuchi K., Matsushita K., Nakazawa K., Ohashi T., Takahashi T., Tamura T., Xu H., 2001, *PASJ*, 53, 401
 Markevitch M., Vikhlinin A., 2007, *PhR*, 443, 1
 Markevitch M., Ponman T. J., Nulsen P. E. J., Bautz M. W., Burke D. J., David L. P., Davis D., Donnelly R. H., Forman W. R., Jones C., and 12 coauthors, 2000, *ApJ*, 541, 542
 Markevitch M., Gonzalez A. H., David L., Vikhlinin A., Murray S., Forman W., Jones C., Tucker W., 2002, *ApJ*, 567, L27
 Markevitch M., Mazzotta P., Vikhlinin A., Burke D., Butt Y., David L., Donnelly H., Forman W. R., Harris D., Kim D.-W., Virani S., Vrtilik J., 2003, *ApJ*, 586L, 19
 Markevitch M., Gonzalez A. H., Clowe D., Vikhlinin A., Forman W., Jones C., Murray S., Tucker W., 2004, *ApJ*, 606, 819
 Mauch T., Murphy T., Buttery H. J., Curran J., Hunstead R. W., Piestrzynski B., Robertson J. G., Sadler E. M., 2003, *MNRAS*, 342, 1117
 Maurogordato S., Cappi A., Ferrari C., Benoist C., Mars G., Soucaïl G., Arnaud M., Pratt G. W., Bourdin H., Sauvageot J.-L., 2008, *A&A*, 481, 593
 McLachlan G. J., Basford K. E., 1988, *Mixture models* (New York: Marcel Dekker)
 Mohr J. J., Mathiesen B., Evrard A. E., 1999, *ApJ*, 517, 627
 Mulchaey J. S., Davis D. S., Mushotzky R. F., Burstein D., 1996, *ApJ*, 456, 80
 Narayan R., Medvedev M. V., 2001, *ApJ*, 562L, 129
 Nulsen P. E. J., David L. P., McNamara B. R., Jones C., Forman W. R., Wise M., 2002, *ApJ*, 568, 163
 O'Sullivan E., Vrtilik J. M., Kempner J. C., David L. P., Houck J. C., 2005, *MNRAS*, 357, 1134
 Owers M. S., Nulsen P. E. J., Couch W. J., Markevitch M., 2009, submitted (arXiv: 0909.2645)
 Paturel G., Petit C., Prugniel Ph., Theureau G., Rousseau J., Brouty M., Dubois P., Cambrésy L., 2003, *A&A*, 412, 45
 Poole G. B., Fardal M.A., Babul A., McCarthy I.G., Quinn T., Wadsley J., 2006, *MNRAS*, 373, 881
 Quintana H., Havlen R. J., 1979, *A&A*, 79, 70
 Randall S. W., Markevitch M., Clowe D., Gonzalez A. H., Bradač M., 2008, *ApJ*, 679, 1173
 Reiprich T. H., Böhringer H., 2002, *ApJ*, 567, 716
 Ricker P. M., 1998, *ApJ*, 496, 670
 Roettiger K., Loken C., Burns J. O., 1997, *ApJS*, 109, 307
 Sakelliou I., Ponman T. J., 2006, *MNRAS*, 367, 1409
 Sanderson A. J. R., O'Sullivan E., Ponman T. J., 2009, *MNRAS*,

- 395, 764
Sarazin C. L., 1986, *RvMP*, 58, 1
Schuecker P., Böhringer H., Reiprich T. H., Feretti L., 2001, *A&A*, 378, 408
Sérsic J. L., 1974, *Ap&SS*, 28, 365
Smith R. J., Hudson M. J., Nelan J. E., Moore S. A. W., Quinney S. J., Wegner G. A., Lucey J. R., Davies R. L., Malecki J. J., Schade D., Suntzeff N. B., 2004, *AJ*, 128, 1558
Struble M. F., Rood H. J., 1999, *ApJS*, 125, 35
Sun M., Murray S. S., Markevitch M., Vikhlinin A., 2002, *ApJ*, 565, 867
Vikhlinin A., Markevitch M., Murray S. S., 2001, *ApJ*, 551, 160
Zakamska N. L., Narayan R., 2003, *ApJ*, 582, 162
Zhang Y.-Y., Finoguenov A., Böhringer H., Kneib J.-P., Smith G. P., Czoske O., Soucail G., 2007, *A&A*, 467, 437

East Sector ^a								
Model	Data	S_0 (cnts cm ⁻² s ⁻¹ arcsec ⁻²)	β	r_c (h_{71}^{-1} kpc)	χ^2/dof
single β	<i>Chandra</i>	$8.85 \pm 0.26 \times 10^{-8}$	0.73 ± 0.02	197.2 ± 5.4	28.5/27
single β	<i>XMM</i>	$7.94 \pm 0.07 \times 10^{-8}$	0.74 ± 0.02	187.0 ± 1.8	41.9/27
West Sector ^b								
Model	Data	$n_{g,1}$ (10^{-3} cm ⁻³)	$\beta_1(\alpha)$	$R_{c1}(R_{cut})$ (h_{71}^{-1} kpc)	$n_{g,2}$ (10^{-3} cm ⁻³)	β_2	R_{c2} (h_{71}^{-1} kpc)	χ^2/dof
A	<i>Chandra</i>	3.95 ± 0.12	4.50 ± 0.12	243.1 ± 4.0	2.60 ± 0.04	0.54 ± 0.01	257.2 ± 2.3	115.1/15
A	<i>XMM</i>	2.90 ± 0.06	2.88 ± 0.06	209.1 ± 4.0	3.08 ± 0.04	0.50 ± 0.01	182.3 ± 1.2	72.5/24
B	<i>Chandra</i>	4.51 ± 0.09	0.07 ± 0.04	111.0 ± 4.4	3.16 ± 0.05	0.63 ± 0.01	238.9 ± 3.3	20.7/15
B	<i>XMM</i>	4.72 ± 0.08	0.03 ± 0.03	104.9 ± 2.2	3.92 ± 0.05	0.66 ± 0.01	200.0 ± 2.1	33.5/24

Table 1. Best-fits to the exposure-corrected surface brightness profiles (Fig. 2b), which are extracted in 0.3 – 2.0 keV from the partial elliptical annuli defined in the east and west sector regions (Fig. 2a). ^a A single β model is sufficient in fitting the SBPs extracted in the east sector (§3.1). ^b Best-fit deprojected spectral parameters obtained in §3.2 (see also Table 2 and Fig. 4e) and two gas density models (§3.3; model A= β component+ β component (Eq. 3); model B=truncated power-law component+truncated β component (Eq. 4)) are used to fit the *Chandra* and *XMM-Newton* profiles extracted in the west sector.

Region ^a	Radius ^b (h_{71}^{-1} kpc)	Data	kT (keV)	Z (Z_{\odot})	χ^2/dof
PROJECTED ^c					
W1	0.0–45.4	<i>Chandra</i>	$5.46^{+0.48}_{-0.31}$	$0.75^{+0.27}_{-0.25}$	119.2/124
		<i>XMM</i>	$5.43^{+0.41}_{-0.30}$	$0.90^{+0.43}_{-0.27}$	124.7/120
W2	45.4–95.3	<i>Chandra</i>	$4.96^{+0.19}_{-0.19}$	$0.69^{+0.14}_{-0.14}$	199.2/206
		<i>XMM</i>	$4.85^{+0.17}_{-0.17}$	$0.81^{+0.13}_{-0.13}$	192.5/207
W3	95.3–136.1	<i>Chandra</i>	$5.42^{+0.33}_{-0.23}$	$0.78^{+0.19}_{-0.18}$	229.4/205
		<i>XMM</i>	$5.53^{+0.29}_{-0.23}$	$0.93^{+0.18}_{-0.17}$	166.2/165
W4	136.1–190.5	<i>Chandra</i>	$5.17^{+0.21}_{-0.21}$	$0.69^{+0.15}_{-0.14}$	212.9/206
		<i>XMM</i>	$5.54^{+0.30}_{-0.32}$	$0.48^{+0.14}_{-0.14}$	187.6/187
W5	190.5–258.5	<i>Chandra</i>	$4.86^{+0.21}_{-0.21}$	$0.58^{+0.15}_{-0.14}$	163.5/126
		<i>XMM</i>	$5.16^{+0.19}_{-0.19}$	$0.63^{+0.14}_{-0.13}$	195.5/216
DEPROJECTED ^d					
W1	0.0–45.4	<i>XMM</i>	$5.71^{+1.04}_{-0.71}$	$0.99^{+0.87}_{-0.70}$	896.3/893
W2	45.4–95.3	<i>XMM</i>	$3.98^{+0.43}_{-0.41}$	$0.58^{+0.37}_{-0.31}$...
W3	95.3–136.1	<i>XMM</i>	$5.38^{+0.74}_{-0.51}$	$1.24^{+0.59}_{-0.50}$...
W4	136.1–190.5	<i>XMM</i>	$5.46^{+1.24}_{-1.17}$	$0.02^{+0.53}_{-0.02}$...

Table 2. Gas temperature and abundance distributions in the west sector region. ^a We divide the west sector region into wider partial elliptical annuli, i.e., W1–W5 regions (Fig. 3a). ^b Equivalent inner and outer radii for each partial elliptical annulus, which are defined as $r = \sqrt{ab}$, where a and b are the corresponding semi-major and semi-minor axes, respectively. ^c An absorbed APEC model is used to fit the *Chandra* ACIS and *XMM-Newton* MOS1+MOS2+pn spectra extracted in the W1–W5 regions. The redshift and absorption are fixed to $z = 0.0597$ and the Galactic value $N_{\text{H}} = 1.62 \times 10^{20}$ cm⁻² (Dickey & Lockman 1990), respectively. Errors are quoted at the 68% confidence. ^d The PROJCT model coded in XSPEC v12.4.0 is used to deproject the *XMM-Newton* MOS1+MOS2+pn spectra. Errors are quoted at the 90% confidence.

Host cluster	1E 0657-56	A754	A2065	A2255	A2256	A3158	A3667
Clump's scale l	(h_{71}^{-1} kpc)	70	120	60	100	160	80 – 110
Projected distance to centre d	(h_{71}^{-1} kpc)	650	200	60	130	130	85
Gas density n_{gas}	(10^{-3} cm ⁻³)	24	4.6	7.2	2.6 – 4.3	4.3	4.5
Gas temperature T	(keV)	7.0 ± 1.0	6.2 ± 0.1	3.4 ± 0.6	5.2 ± 0.7	4.5 ± 1.0	4.0 ± 0.4
Ambient temperature T_{amb}	(keV)	13.6	7.4	5.5	6.9	6.7	5.5
Cluster temperature T_{cluster}	(keV)	13.6 ± 1.0	10.0 ± 0.3	5.5 ± 0.2	6.9 ± 0.3	6.7 ± 0.2	5.5 ± 0.1
Metal abundance Z	(Z_{\odot})	...	0.54	1.36	...	0.84	0.81
Cooling time t_{cool}	(10^9 yr)	2.4	12.0	5.7	11.7 – 19.4	10.9	9.8
Effective conduction time t_{cond}	(10^9 yr)	0.1	0.3	0.3	0.2 – 0.3	0.7	0.3 – 0.6
Gas mass M_{gas}	($10^{11} M_{\odot}$)	1.1	1.0	0.2	0.3 – 0.6	2.3	0.3 – 0.8
Gas entropy S	(keV cm ²)	84 ± 12	224 ± 4	91 ± 16	236 ± 80	170 ± 38	147 ± 15

Table 3. Properties of the massive, off-centre cool gas clumps, which are detected in 1E 0657-56 (Markevitch et al. 2002), Abell 754 (Markevitch et al. 2003; Henry et al. 2004), Abell 2065 (Chatzikos et al. 2006), Abell 2255 (Sakelliou & Ponman 2006), Abell 2256 (Sun et al. 2002), and Abell 3667 (Vikhlinin et al. 2001; Briel et al. 2004), respectively. Cooling times of the cool clumps are calculated from Eq (5), and effective conduction times are estimated from Eq (6) by assuming a tangled magnetic effect. Gas masses of the cool clumps are calculated by assuming that the gas density, temperature, and metal abundance are constant in the clump. Gas entropies are given by $S = kT/n_{\text{gas}}^{2/3}$.

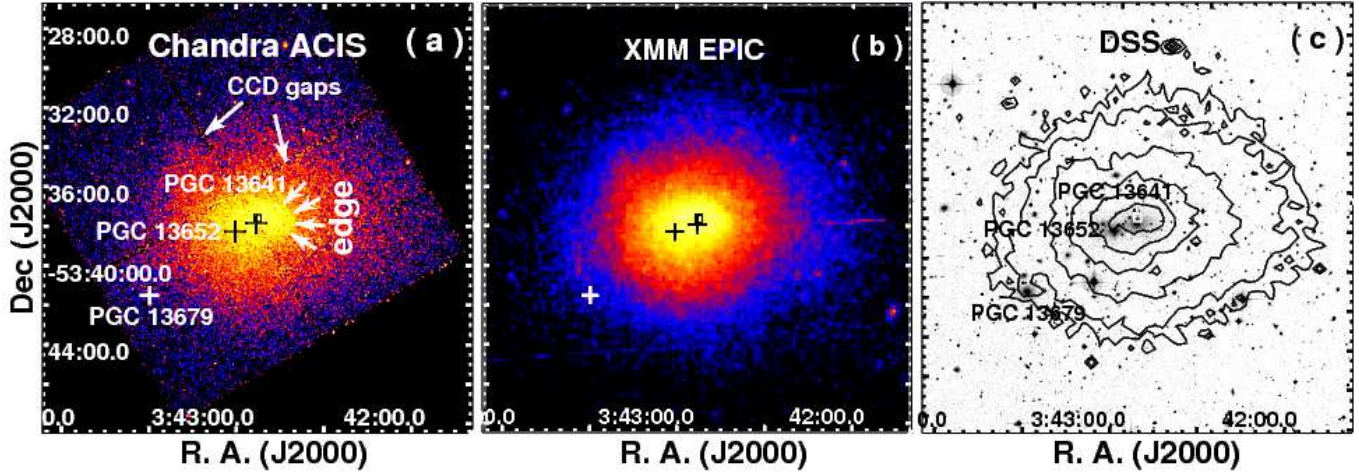


Figure 1. (a)–(b) Adaptively smoothed and exposure-corrected *Chandra* ACIS-I (ObsID 3712) and *XMM-Newton* EPIC (ObsID 0300210201) images of the central $1.5h_{71}^{-1} \text{ Mpc} \times 1.5h_{71}^{-1} \text{ Mpc}$ ($21'.93 \times 21'.93$) region of Abell 3158. Both images are extracted in 0.3–2.0 keV and plotted in logarithmic scale. One small box and three crosses are used to mark the peak of the X-ray halo and the centres of luminous member galaxies PGC 13641, PGC 13652, and PGC 13679, respectively. (c) Optical DSS *B*-band image for the same sky field as (a) and (b), on which the *Chandra* X-ray intensity contours (square root scale) are plotted.

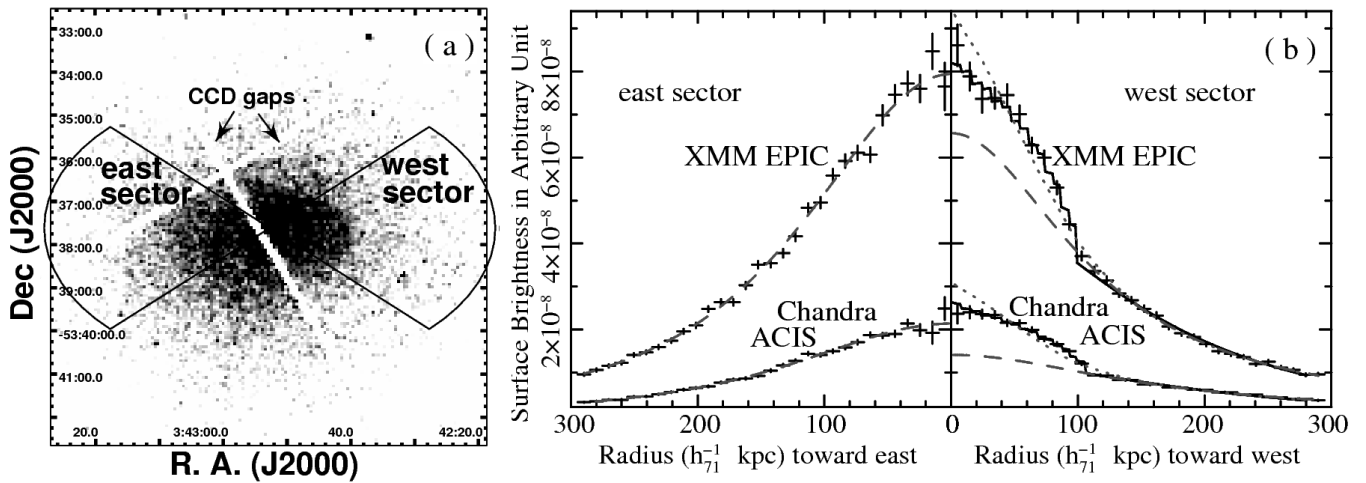


Figure 2. (a) East and west sector regions used to extract the X-ray SBPs, which are shown in (b). Here the *Chandra* ACIS image is used as the background image. (b) *Chandra* ACIS and *XMM-Newton* EPIC 0.3–2.0 keV SBPs extracted from the partial elliptical annuli defined in the two sector regions. For SBPs extracted in the east sector, a single β model can give an acceptable fit to the observed SBPs (dashed lines; §3.1 and Table 1). For SBPs extracted in the west sector, dashed, dotted, and solid lines are used to show the best-fits obtained with the single β model (§3.1), two- β model, and truncated powerlaw+ β model (§3.3 and Table 1), respectively.

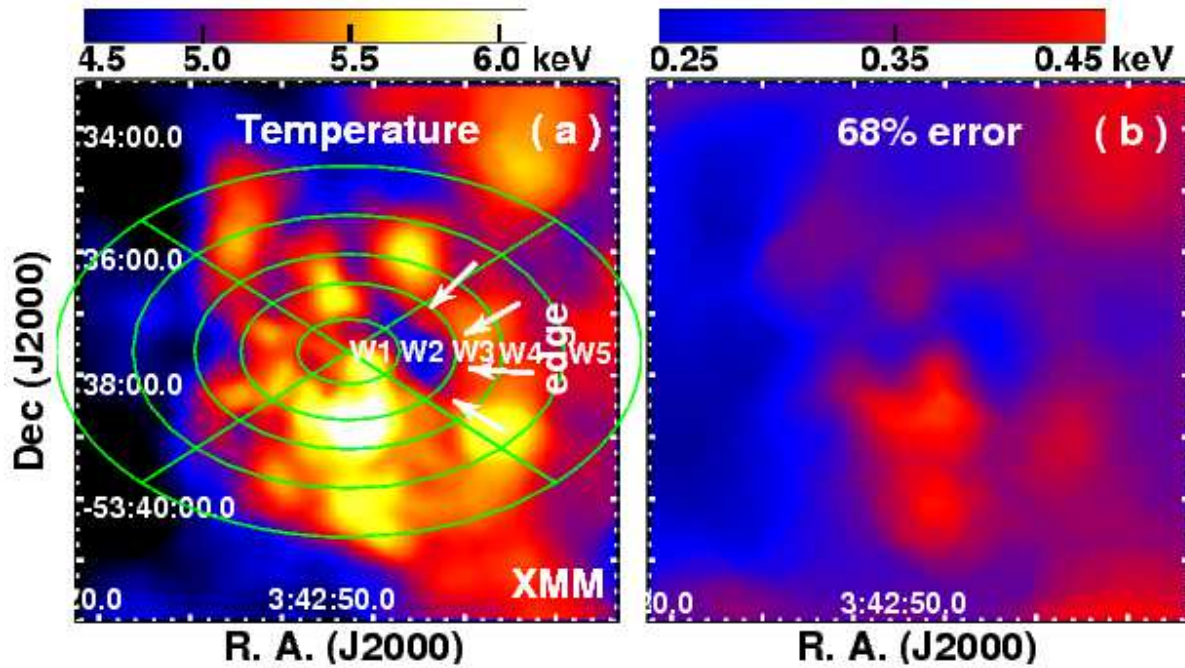


Figure 3. (a) Projected gas temperature map for the central $0.6h_{71}^{-1} \text{ Mpc} \times 0.6h_{71}^{-1} \text{ Mpc}$ ($8'.77 \times 8'.77$) region, along with the 68% error map (b), which are calculated from the *XMM-Newton* MOS1+MOS2+pn data. Partial elliptical annuli defined in the north, east, south, and west sector regions are shown in (a), which are used to extract both the *Chandra* and *XMM-Newton* spectra to be analysed in §3.2.

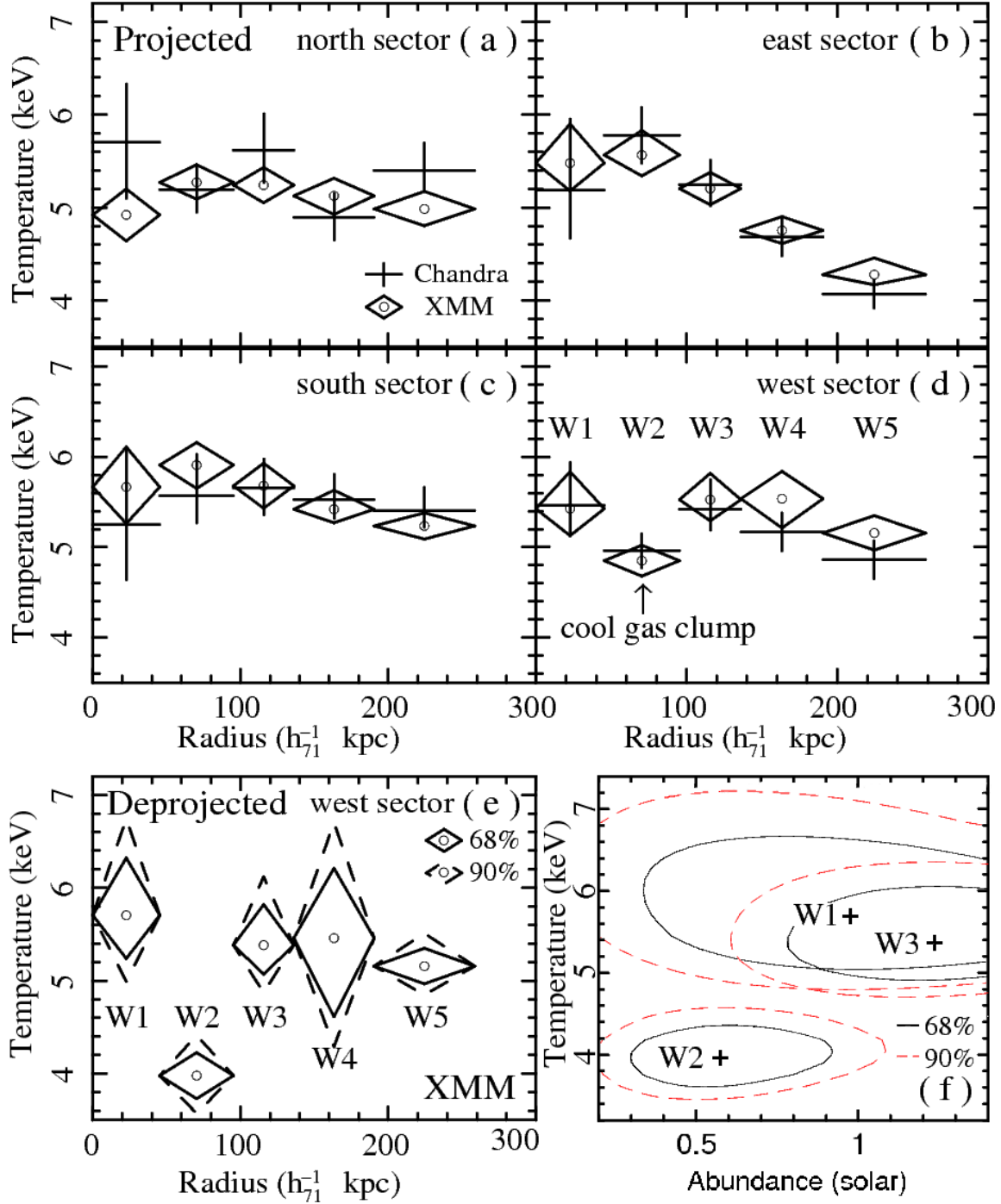


Figure 4. (a)–(d) Projected gas temperature profiles obtained with *Chandra* ACIS (cross) and *XMM-Newton* MOS1+MOS2+pn (diamond) data for the north, east, south, and west sectors defined in Fig. 3a, along with the 68% errors. (e) Deprojected *XMM-Newton* temperature profiles for the west sector, along with the 68% (solid) and 90% (dashed) errors (see also Table 2). (f) Fit-statistic contours of temperature and abundance at the 68% ($\Delta\chi^2 = 2.30$; solid) and 90% ($\Delta\chi^2 = 4.61$; dashed) confidence levels for the inner three partial annuli of the west sector, all obtained in the *XMM-Newton* deprojected analysis.

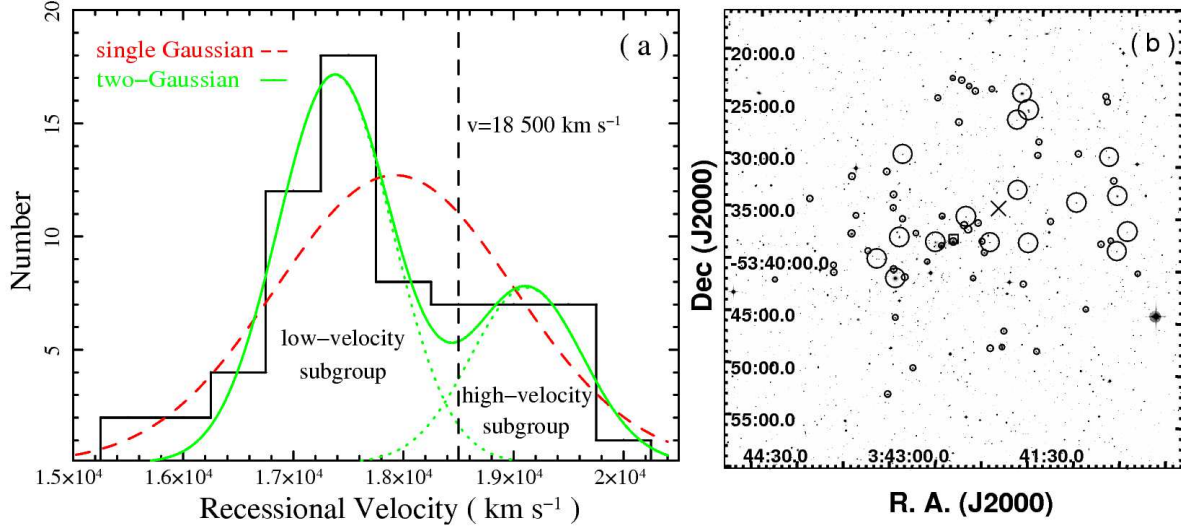


Figure 5. (a) Line-of-sight velocity distribution of 68 member galaxies identified in Abell 3158. Original velocity data are drawn from Smith et al. (2004). The distribution is fitted with a two-Gaussian model (solid) and a single Gaussian model (dashed; §4), respectively. (b) DSS optical image for the central $3.0h_{71}^{-1}$ Mpc \times $3.0h_{71}^{-1}$ Mpc ($43'.86 \times 43'.86$) region of Abell 3158, where the low-velocity ($v < 18\,500$ km s $^{-1}$) and high-velocity ($v > 18\,500$ km s $^{-1}$) member galaxies are marked with small and large circles, respectively. The X-ray peak is marked with a small box and the geometric centroid of the high-velocity subgroup is marked with a cross.

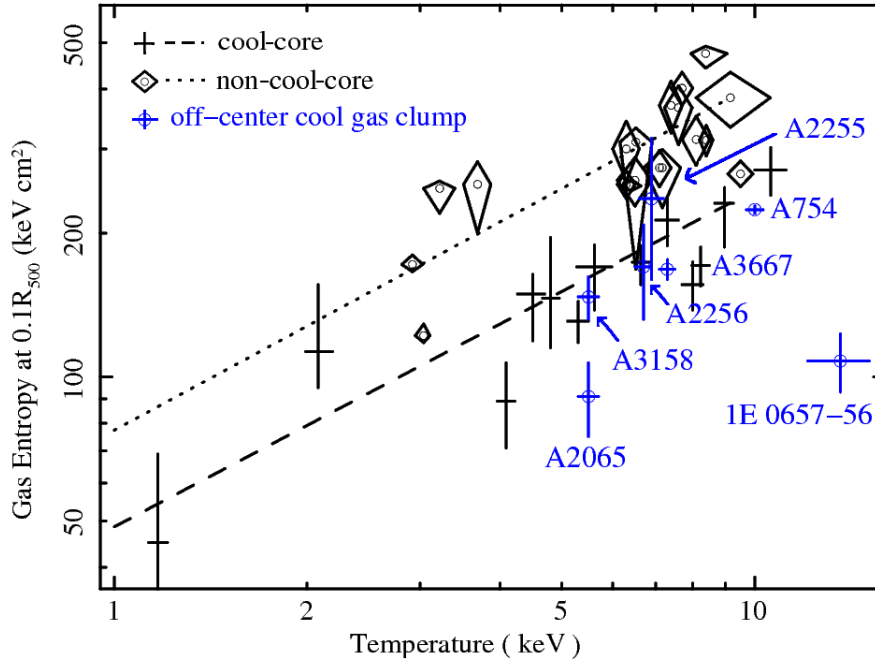


Figure 6. Redshift-corrected gas entropy measured at $0.1R_{500}$ (roughly 50 – 150 kpc) vs average gas temperature for cool-core clusters (crosses) and non-cool-core clusters (diamonds), which are re-calculated based on the data of Zhang et al. (2007) and Sanderson et al. (2009). The corresponding best-fit power law models given by Sanderson et al. (2009) are also shown as dashed and dotted lines, respectively. The entropy-temperature distribution of the off-centre cool gas clumps (Table 3) is also plotted.